A New Method for Polar Field Interpolation

X. Sun[1,2] · **Y. Liu**[1] · **J. T. Hoeksema**[1] ·
K. Hayashi[1] · **X. Zhao**[1]

Abstract The photospheric magnetic field in the Sun's polar region is not well observed compared to the low-latitude regions. Data are periodically missing due to the Sun's tilt angle, and the noise level is high due to the projection effect on the line-of-sight (LoS) measurement. However, the large-scale characteristics of the polar magnetic field data are known to be important for global modeling. This report describes a new method for interpolating the photospheric field in polar regions that has been tested on MDI synoptic maps (1996-2009). This technique, based on a two-dimensional spatial/temporal interpolation and a simple version of flux transport model, uses a multi-year series of well-observed, smoothed north (south) pole observation from each September (March) to interpolate for missing pixels at any time of interest. It is refined by using a spatial smoothing scheme to seamlessly incorporate this filled-in data into the original observation starting from lower latitudes. For recent observations, an extrapolated polar field correction is required. Scaling the average flux density from the prior observations of slightly lower latitudes is found to be a good proxy of the future polar field. This new method has several advantages over some existing methods. It is demonstrated to improve the results of global models such as the Wang-Sheeley-Arge (WSA) model and MHD simulation, especially during the sunspot minimum phase.

Keywords: Magnetic fields, Photosphere; MDI: synoptic maps; Polar region

1. Introduction

The observed photospheric magnetic field, in the form of line-of-sight (LoS) magnetograms assembled into synoptic maps, has been used to model the coronal field for more than 30 years (Schatten, Wilcox, and Ness, 1969; Hoeksema, 1984; Wang and Sheeley, 1990; Linker *et al.*, 1999). The global field serves as the boundary condition, which is essential to most coronal and interplanetary models. Although a lot of effort have been devoted to improve the data quality,

[1] W. W. Hansen Experimental Physics Laboratory, Stanford
University, Stanford, CA 94305.
Email: xudongs@stanford.edu
[2] Department of Physics, Stanford University, Stanford, CA
94305

many issues are still not fully resolved. One of them is the quality of magnetic field in the polar regions.

The polar region typically has a field of predominantly one polarity and it accounts only for a small fraction of the solar surface, just 3.4% above 75° latitude. Because the unipolar caps are the source of the stable polar coronal holes, the magnetic field from this region proves to be crucial to large-scale modeling efforts (Arge and Pizzo, 2000; Luhmann *et al.*, 2009). Due to the Sun's tilted rotation axis relative to the ecliptic and the line-of-sight nature of the magnetic field observations, there are data missing or poorly measured at one or both poles throughout the year, and the noise level is relatively high. This paper describes a new interpolation method (a.k.a. "polar field correction") for estimating the problematic values in the polar region. The method can be applied to interpolate historic values and extrapolate future field strength. We note that any such polar field correction method is designed for the study of long-lived, global, large-scale magnetic field. Individual small-scale structures of the photospheric field, such as rapidly evolving magnetic elements, are not as important for global field models and are beyond the scope of this study.

Section 2 presents a brief overview of the MDI magnetic field synoptic maps. We use that to illustrate the problems we face with polar field observation. A summary of several existing interpolation schemes is presented in Section 3, followed by a detailed description of the new method. To validate this method, we prepare MDI maps processed with the new method as well as some of the old methods and apply them to the Wang-Sheeley-Arge (WSA) model (Arge and Pizzo, 2000) and a daily MHD simulation (Hayashi, Zhao, and Liu, 2008). A comparison of results is shown in Section 4.

2. MDI Synoptic Map and Its Polar Field

Longitudinal photospheric field is observed from the Earth or from one point (L1) in space. Full-disk magnetograms are most commonly presented as near-side images of the LoS field component. In order to provide the global distribution of magnetic field as a boundary condition for solar models, we remap the magnetograms with proper calibration onto heliographic coordinates. Magnetograms observed at different times are de-rotated to account for differential rotation, registered to the appropriate Carrington coordinates, and averaged within a certain-sized time window to beat down the noise. These remapped, averaged magnetograms collected over a solar rotation contribute to a "global map" of the solar magnetic field (synoptic maps). In this process we assume that the large scale structure of the photospheric field is relatively stable within the time scale of one Carrington rotation (CR), so the observed value at one instant can more or less represent the local magnetic condition for the whole rotation. This is generally true except for fast evolving active regions (Zhao, Hoeksema, and Scherrer, 1999).

SOHO/MDI provides full disk magnetograms with 96-minute cadence (Scherrer *et al.*, 1995). These magnetograms have been corrected for zero-point offset following the method described by Liu, Zhao, and Hoeksema (2004) and rescaled

for sensitivity according to Tran *et al.* (2005) since the values in MDI magnetograms are shown to be underestimated (Berger and Lites, 2003; Tran *et al.*, 2005). Each calibrated magnetogram is then mapped from image coordinates onto a regular Carrington coordinate grid using a cubic convolution interpolation method. Differential rotation is also taken into account (Meunier, 2005). The line-of-sight field values are converted to radial field values at the same time under the assumption that MDI is measuring the LoS component of a purely radial field. This also removes the projection effect due to the inclination of the solar equator (the solar B_0 angle). To avoid high noise due to projection, we discard data from the edge of the solar disk in a magnetogram (outside 0.995 disk radius). For each pixel in the synoptic map, we identify the corresponding pixels in the remapped magnetograms that were observed closest to the central meridian passage. Pixels from a certain number of Level 1.8 magnetograms (20 "effective points", with those from 1-min cadence magnetograms counting for 1, and 5-min counting for 2.75) are finally averaged to determine the value of that point in the synoptic map. Data in the final maps are generally observed within $10°$ of central meridian.

MDI full rotation magnetic synoptic maps (http://soi.stanford.edu/magnetic/index6.html) have a 3600×1080 pixel resolution. The x-axis is in Carrington longitude and y-axis in sine latitude. In these maps, each pixel represents the same surface area on the Sun. The maps are available in two formats: LoS field and radial field. The LoS field is computed from the radial synoptic map, under the assumption that the photospheric field is radially directed (Wang and Sheeley, 1992). Besides these two, the MDI project also produces daily-updated synoptic frames. Data from the newest magnetograms are incorporated to the leading edge (left) of the synoptic map. As the result, the left edge of the map consists of fewer magnetograms than the right edge and the data are observed farther from central meridian. These maps reflect the latest magnetic conditions observed simultaneously over a large portion of the Sun and are especially suitable for space weather forecasting (Arge and Pizzo, 2000).

The inclination of the Sun's rotation axis with regard to the normal of the ecliptic can be as large as $7.25°$. The north (south) pole is not observable during March (September) when it tilts away from the Earth. Consequently, missing data appear in the synoptic maps in the north (south) polar region while the other pole can be somewhat better observed. Also, since line-of-sight field measurements of essentially radial field in pixels on the edge of the solar disk in magnetograms are too noisy to be used, there can be as many as 16 rows of pixels missing from the upper/lower edge of the MDI synoptic maps. Figure 1(a) shows a stereoscopic polar view of the magnetic field during CR1920 (March 1997) and CR1924 (July 1997). Black region indicates missing data.

The measured LoS component of the field has a nearly uniform noise level at different latitudes. However, in practice the radial field synoptic map is typically used as model input (Wang and Sheeley, 1992). In the conversion process mentioned above, LoS field is considered to be the projected component of the radial field. As consequence, the inferred radial field will be greatly amplified in the polar region relative to the observed LoS field. Noise level thus also increase drastically in the polar region. Modeling output often becomes unstable or unreasonable without proper treatment of the noisier polar field (see Section 4).

3. Interpolation Methods

3.1. Brief Review of Existing Methods

Seven different polar field interpolation methods have been studied and compared in Liu *et al.* (2007). We briefly summarize these methods.

1. *One-dimensional cubic spline interpolation.* four successive observed pixels are chosen from each column in the data array at one longitude adjacent to the missing data area. Another four pixels are chosen 180° away in longitude in the same fashion. A cubic-spline interpolation is performed with four known pixels at each end and the interpolated values are used for the polar region.
2. *Modified one-dimensional cubic spline interpolation.* Similar to method 1. The original map is smoothed before the interpolation.
3. *Spherical harmonic smoothing method.* The one-dimension cubic spline interpolation (method 1) is performed on the original map first. A spherical harmonic expansion is performed and high-order components are truncated. The reconstructed, smoother field with only lower-order components is used for the polar region.
4. *Two-dimensional spatial interpolation.* Observed data from lower latitudes of each hemisphere are fit with a third-order two-dimensional polynomial function by using the least-square technique. The fit values are used for the missing data.
5. *Two-dimensional temporal interpolation.* Each year, about a month of the polar data centered at 8 September (6 March) for north (south) pole is used. The Sun's tilt angle reaches maximum at those two times and the pole becomes better observed. After fitted with a polynomial function (same as method 4), these annual data form a temporal series that can be used to interpolate for field strength at any given time.
6. *Polar field model method.* A "topknot" polar field modeled by Svalgaard, Duvall, and Scherrer (1978) is used (see also, Wang and Sheeley, 1988). In this model $B_r = B_p \cos^n \theta$, $B_\theta = B_r \tan(q\theta)$, where B_p is the field strength at the very pole, and θ is the colatitude. Free parameters n and q are determined using observations from the Wilcox Solar Observatory (WSO) as $n = 8$ and $q = 0$. In this way, the polar field is entirely determined by the value of B_p. Each year, the best observed polar field (as mentioned in method 5) is longitudinally averaged above 65° and fitted for B_p. These annual values of B_p can be used to interpolate B_p and construct the polar field for any desired time.
7. *Method based on Flux Transport model.* Polar field determined from a flux transport model (Schrijver and DeRosa, 2003) is adopted. This model includes the effect of differential rotation, meridional flow and supergranular random-walk dispersal. If available, MDI magnetograms are assimilated within 60° from disk center every 6 h. When the 180° longitude of a synoptic map passes the central meridian, assimilated polar field data at this instant of time is used to fill out the polar region of the very map.

In Liu *et al.* (2007), these methods were applied to a set of nine MDI synoptic maps that were used for potential-field source-surface (PFSS) computations. Three of these nine maps were taken from the solar cycle minimum phase, three from the maximum phase, three from the declining phase. The computed open field line foot-points and the heliospheric current sheet location were compared with observations, such as coronal hole maps from Kitt Peak (He I 1083 nm) and measurements of the interplanetary magnetic field (IMF) polarity at 1 AU.

Overall, the two-dimensional temporal interpolation (method 4) gave the best result. Similar but slightly less satisfying results were obtained from method 5 and 7. Some of these models prove to be sensitive to the noise signal in the original map and are error-prone. For example, the one-dimensional cubic spline interpolation method does not give very reasonable foot-point configurations for the test Carrington rotations, because the interpolation heavily depends on the pixels we choose. If the chosen pixels happen to fall in some magnetic elements, the interpolated values will then be unreasonably high. We will see an example of this in Section 4.

In most of these methods, the actual area being interpolated varies from rotation to rotation during the year. For instance, during July (CR1924) when both poles have missing data, both poles will be corrected. However, during March (CR1920) when the south pole is well observed, only the north pole will be corrected. Clearly the two poles will then have different noise levels. We note that using unsmoothed polar data can lead to unreasonable modeling result even when they are well observed (see Section 4). Furthermore, simple interpolation will leave discontinuities at the boundary of original and interpolated data. This is because the filled-in values are usually smoothed, while the original data are noisier. These issues are worth considering when we design a new interpolation method.

3.2. The New Method

A good polar field interpolation method should be able to 1) give a reasonable estimate of missing data and 2) lower the noise by smoothing to prevent biased modeling results. An objective, self-consistent method that processes *all* synoptic maps with a *single* standard process is preferred. It is also desirable to utilize as much of the good-quality observed data as possible.

We base the new polar field correction scheme on the two-dimensional spatial and temporal interpolation methods (methods 4 and 5) and implement a few key improvements. For extrapolation, we incorporate a simple variation of the flux transport model (method 7) which is described in Section 3.3. Figure 1 shows the corrected polar field for CR1920 and CR1924 as a comparison with the original data.

Three major issues remain for the original spatial/temporal interpolation methods. 1) The observed data at the polar regions that are used for fitting or smoothing vary in quality themselves. If one pole is tilted away from the Earth, we will have to use fewer/noisier pixels to estimate more missing pixels. This is likely to result in very different data quality at two poles in a map, and also from map to map. 2) The missing/noisy pixels in the polar region are

usually directly replaced by fitted/smoothed values, a discontinuity in noise level is usually unavoidable. 3) The method needs to provide an extrapolated result for modeling the present as well as interpolated results for historical study. As we will see in Section 4, not addressing these issues may lead to unreasonable model result.

Therefore, we design and describe the following procedures.

Step 1: *Estimate the higher-latitude data based on the best polar observations during the year.* Figure 2(a) illustrates this step. Instead of fitting directly from current low-latitude data that vary in quality, we make use of the best polar observations available at 8 September (6 March) each year for north (south) pole. A total of 13 annual north (south) polar observations are thus gathered from 1996 to 2009 (excluding the "SOHO vacation" in summer 1998). We smooth the well-observed data above 62° using a seventh-order polynomial function. The third-order polynomial originally used in Liu *et al.* (2007) does not seem to reproduce enough variations in the large scale field strength for the full-resolution maps. These smoothed data are aligned according to Carrington coordinate, so pixels with the same Carrington coordinates form a time series. We then use this annual time series and perform a temporal one-dimensional cubic spline interpolation to synthesize the values above 75° latitude, for *both* poles in *each* map.

Step 2: *Merge the synthetic data with the original observation.* At this stage the polar data consist of two parts: the original observation below 75° latitude, and the smoothed, evolved, filled-in data above that as shown in Figure 2(b). In order to minimize the discontinuity between them, the same two-dimensional smoothing is first performed on this two-part polar data above 62° latitude to create a smoothed polar "mask" for each rotation. To produce the final polar field, pixels above 75° latitude are directly taken from the mask. Between 62° to 75° we make a linear combination of the mask data and the original unsmoothed observations, their weight linearly increases with latitude from 0 to 1 (or decreases from 1 to 0). As a result, the noise level gradually decreases from 62° to 75° without apparent discontinuity.

3.3. Notes on the New Method

Figure 3 shows the average radial field strength of the well-observed polar data above 75° latitude observed during each favorable season. As net new flux is gradually transported from lower latitudes, the flux density changes gradually from one year to the next. Note that due to the small size of the polar region, most global models respond sensitively only to the average value of the field, and do not so much depend on the detailed spatial flux distribution. The simple interpolation we use here reflects this gradual change of flux density and thus provides an adequate estimate of the missing pixels.

The well observed polar field data are assembled from standard synoptic maps that have a nominal resolution of 3600 in longitude and 1080 in sine latitude. The polar strips are 63 pixels high to include the region above 62° latitude. The latitude range is chosen according to the polar coronal hole size during the past sunspot minimum, which usually has a 30° extent in latitude. The strips

are significantly extended in longitude to account for differential rotation. Strips span 429° in Carrington longitude (about 32.5 days) in accordance with the differential rotation rate at 75° latitude (Meunier, 2005). As the polar region rotates more slowly, this extra 5.2 days (compared with the nominal 27.3 day Carrington period) allows us to include information for the Sun's entire polar region.

Above 75° latitude (the top and bottom 18 rows) the values are simply replaced by the temporally interpolated data. This range is only slightly larger than the extreme cases where there can be 16 rows missing from the polar region of the synoptic map. The replacement is made for *both* poles and *all* synoptic maps to keep the noise level comparable for the two poles in each map, as well as for the same pole in different maps.

Because observations of the following September/March are not yet available when considering recent time intervals, an interpolation method cannot be used for the correction of up-to-date maps. A reliable extrapolation scheme must be developed to estimate the missing data. The results for several regular extrapolation methods (spline, quadratic, linear, sinusoidal, *etc.*) are shown by the indicated symbols in Figure 3. Starting yearly in 2000, we extrapolate the averaged flux density of north/south pole based on the prior observation series. The extrapolated value depends heavily on a few points proceeding the desired time, so the prediction is prone to diverge from the actual observation whenever the evolution of the polar field deviates from what is described by the extrapolation function. This is especially true for this deep sunspot minimum when the polar field remained significantly weaker for a longer period than the previous ones (*e.g.* in September 2006).

The best prediction uses the average flux density in the slightly lower latitude range between 62° and 75° from previous year. The result, multiplied by 1.1 (in filled black square/diamond), is much better correlated with the observed values (open square/diamond). Therefore we use this lower-latitude average value to scale the most recent September/March observation and use the scaled data as the "projected" observation for the upcoming September/March. A regular temporal interpolation can then be performed. When new September/March observations eventually become available, we substitute the "projected" observation with the measured values. This means we will update the polar field values for the past year twice every year, in late March and September.

Like other polar field interpolation schemes, the two polar regions we have defined may not be in flux balance, as shown by the dashed line in Figure 3. It is hard to tell how much of the residue is an artifact of the process and how much represents a real local imbalance. Systematic differences in the instrument or the specification of our polar geometry parameters may also play a role. The apparent monopole component of the full maps, which is typically discarded during modeling, may sometimes cause a significant shift of field inversion line location in the upper corona and lead to erroneous results. Quantitatively, the net flux in the corrected polar regions has a maximum average field strength of about 2 gauss (G) in the polar region during sunspot maximum, and is very close to 0 during most other times. A 2 G average above 75° is equivalent to global offset of less than 0.1 G. An offset of this magnitude is of less importance during

the maximum phase due to the greater influence of the stronger high-order field components. The global coronal structure is more likely to be affected by the evolution and eruption of strong active regions.

4. Validation and Discussion

4.1. Wang-Sheeley-Arge Model

We use polar field corrected MDI synoptic maps as the input to the Wang-Sheeley-Arge (WSA) model for solar wind prediction (X. Sun, Private communication). Following the method described by Arge *et al.* (2004), we predict the three-day advanced solar wind speed at L1 from 1996 to 2009 (CR1912 to CR2084). In brief, a potential-field source-surface (PFSS) model is used to compute the coronal field configuration between the photosphere and 2.5 $R_\odot$ source surface. Two parameters are calculated: the flux-tube expansion factor (f_s) (Wang and Sheeley, 1990) and the angular separation between the open field line foot-point and the nearest edge of the coronal hole (θ_b) (Riley *et al.*, 2001). Arge *et al.* (2004) proposed an empirical function that uses these two parameters to predict the solar wind velocity near the Sun. The specific coefficients used to make the prediction must be iteratively determined for each synoptic data source by comparing the 1 AU predictions and observations. We adopt a trial-and-error scheme and statistically evaluate performance of each trial coefficient set, as described below. The best set of coefficients is chosen for the model. For MDI, we use the following relationship:

$$v = 265 + \frac{1.5}{(1 + f_s)^{0.22}}[6.1 - 1.2\exp(1 - (\frac{\theta_b}{2.5})^{1.5})]^{3.4} \text{ (km s}^{-1}), \qquad (1)$$

where f_s is the flux tube expansion factor, and θ_b is the angular separation. A one-dimensional kinetic model is used in this process to map these values at the source surface forward to the Earth.

The predicted solar wind speed at L1 is evaluated by comparing with the OMNI observations (King and Papitashvili, 2005) on a point-by-point basis. The prediction time series and the OMNI hourly data are first interpolated/averaged to the same temporal resolution. Four statistical metrics are studied: root-mean-square error of the predicted speed (RMSE), mean absolute percentage error (MAPE), correlation coefficient between the predicted and observed speed (CC), and the success rate of IMF polarity prediction (PIMF). Since these metrics are also used to optimize the empirical equation, the model result essentially estimates the model's best statistical performance on solar wind prediction.

The first row of Table 1 shows the statistics for the prediction with a 4.5-hour resolution (corresponding to the 2.5° input resolution). The model gives an overall 96.8 km s^{-1} RMSE, which is equivalent to a 15.9% error. The predicted velocity time series has a correlation coefficient of 0.470 with the observed series. The IMF polarity prediction is correct 81.2% of time. If we interpolate our prediction to a 1-hour resolution per Owens *et al.* (2008), the same analysis

shows a RMSE of 92.3 km s^{-1} between 1996 and 2002, comparable to the result (94.9 km s^{-1}) given in the same paper (for 1995-2002).

To demonstrate the effect of the new correction scheme, synoptic maps with the polar correction based on the one-dimensional interpolation method described above are also evaluated using the same procedures. As shown in Table 1, the new polar field method improves the model's performances in all four categories. The improvement is especially pronounced during the sunspot minimum phase when the polar fields are strongest and most uniform. We compare two versions of mean-square error of speed, through the index of "skill score" :

$$\text{skill} = (1 - \frac{\text{MSE}}{\text{MSE}_{\text{ref}}}) \times 100, \qquad (2)$$

where we use the MSE of the 1D interpolated version as the reference. Figure 4(a) shows the RMSE value of two methods. Each point represents the RMSE of data within a one year window and the points are sampled every half a year. The skill score of MSE for the new method compared to the 1D method is shown in Figure 4(b). It can be as high as 46.7 (improvement of 46.7%) during the solar minima, with an average of 14.4 over the solar cycle. The long-term, overall accuracy of solar wind prediction is improved after we apply the new method. We notice that from 1999 to 2001, when the polar field was near zero, the new method yields slightly worse result than the 1D interpolation result. It might be because the polar field does not change smoothly due to the arrival of new flux in the form of "magnetic surges", which makes the new method inaccurate. Nevertheless it is hard to determine the cause because the effect of polar field is less dominant during the maximum phase and more transient ejecta start to affect the background solar wind flow.

Figure 4(c) and 4(d) show a similar comparison for PIMF. The skill score is now defined as

$$\text{skill} = (\frac{\text{PIMF}}{\text{PIMF}_{\text{ref}}} - 1) \times 100, \qquad (3)$$

as higher PIMF indicates better accuracy. Again, we use the result from 1D interpolation as reference. Although the time variation of PIMF is very different from RMSE, the skill score shows a similar trend, being the highest during the recent minimum (about 15%). The 1D interpolation sometimes preduces biased polar field strength which distorts the shape and location of the heliospheric current sheet, leading to erroneous IMF polarity prediction. It is clear that a good estimate of the polar field is crucial to the models during solar minimum period.

In the WSA model, sources of solar wind are identified by mapping field lines back to the photosphere from the corona, as solar wind is accelerated along flux tubes. In Figure 5(a), the top two plots show the north pole view of magnetic field synoptic map above 60° latitude for CR 1920. The left plot is computed based on data processed with the new method, the right one shows the result for the one-dimensional interpolation. The bottom two show the computed open field regions from these two maps. The color indicates the predicted solar wind speed. Figure 5(b) shows the same for south pole. (Since the south pole is well

observed during this time, no correction is required at the south pole for the 1D method.) As mentioned in Section 2, even though the south pole is well observed, noisy data with large flux of the opposite polarity can still lead to large-scale closed field structures. Large-scale low-speed solar wind streams appears at the center of the large polar coronal hole, which disagrees with the concurrent Ulysses observations during sunspot minimum (Neugebauer *et al.*, 1998). For the north pole when the data are even noisier, a simple 1D interpolation yields even worse result. The smoothing scheme used in the new method has prevented this unreasonable modeling outcome.

4.2. MHD Simulation

The new polar interpolation method also proves to be useful for MHD simulations. In order to study the real-time solar corona conditions, we incorporate the MDI daily-updated synoptic maps into a time-relaxation MHD simulation (Hayashi, 2005; Hayashi, Zhao, and Liu, 2008). For this near real time exercise, the MHD code employs the polytropic assumption with a specific heat ratio of 1.05. This choice of specific heat generally yields lower solar wind speeds than observation, but reproduces realistic stream structures that can be directly compared with observations. The simulation result is sensitive to the input data, thus ideal for this test.

Daily-updated synoptic maps that include the information from the latest magnetograms are used as the inner boudary and the simulation is run on a daily basis (http://sun.stanford.edu/~keiji/daily_mhd/daily_mhd.html). The data are binned from the 360×180 daily-updated MDI synoptic map to a 72×30 resolution map for MHD computation. Each pixel in the low-resolution map is simply the average of an evenly-spaced 5×6 window in the original map.

We use two sets of synoptic maps as input. The first set is treated with the new interpolation method and then binned to lower resolution. The second set does not have any specific polar field interpolation; if there are missing pixels in the binning window, we simply use the average of existing pixels in that window. Figure 6 shows the simulated solar wind velocity at the height of 2.525 $R_\odot$, for 25 and 26 February, 2008. The center of each map has been shifted so the left edge is placed at Carrington longitude $0°$ of a certain rotation. The left edge of the original map is denoted by the vertical dotted line.

We expect the wind speed distribution to be largely stable over a period of two days. Both poles should produce high speed wind since it is during sunspot minimum phase. However, in Figure 6, the lower row that with no polar field correction contradicts the postulate. The poorly observed north pole produces solar wind that is much slower than the south pole, and the predicted speed distribution changes drastically from one day to the next. Detailed analysis suggests that the noisy polar field data on the upper-left edge of the input map are responsible for this result. The location of the inferred current sheet (zero radial field) also shifts due to the changing of flux imbalance from the two poles. In this occasion, the upper row that utilizes the new method gives a far more reasonable answer.

4.3. Summary

We describe a new polar field interpolation scheme for the MDI synoptic maps. The method relies on well-observed polar data during September/March each year to estimate the time varying large-scale polar field and then merges the synthesized field back smoothly into the original map. The same procedure is applied to both poles and to all maps so the noise level at the poles remains comparable over time. For global models such as the WSA model and daily MHD simulation, the method is shown to improve the result when compared with some existing methods.

MDI synoptic maps with polar field corrected in this fashion are available as a standard product on the MDI website (http://soi.stanford.edu/magnetic/index6.html). We plan to apply the same method to the Helioseismic and Magnetic Imager (HMI) synoptic maps, after we study and compare the data in detail with MDI.

References

Arge, C.N., Pizzo, V.J.: 2000, Improvement in the prediction of solar wind conditions using near-real time solar magnetic field updates. *J. Geophys. Res.* **105**, 10465.

Arge, C.N., Luhmann, J.G., Odstrčil, D., Schrijver, C.J., Li, Y.: 2004, Stream structure and coronal sources of the solar wind during the May 12th, 1997 CME. *J. Atmos. Solar-Terr. Phys.* **66**, 1295.

Berger, T.E., Lites, B.W.: 2003, Weak-field magnetogram calibration using advanced stokes polarimeter flux density maps - II. soho/mdi full-disk mode calibration. *Solar Phys.* **213**, 213.

Hayashi, K.: 2005, Magnetohydrodynamic simulations of the solar corona and solar wind using a boundary treatment to limit solar wind mass flux. *Astrophys. J. Suppl.* **161**, 480.

Hayashi, K., Zhao, X., Liu, Y.: 2008, MHD simulations of the global solar corona around the Halloween event in 2003 using the synchronic frame format of the solar photospheric magnetic field. *J. Geophys. Res.* **113**, 7104.

Hoeksema, J.T.: 1984, Structure and evolution of the large scale solar and heliospheric magnetic fields. PhD thesis, Stanford University.

King, J.H., Papitashvili, N.E.: 2005, Solar wind spatial scales in and comparisons of hourly wind and ACE plasma and magnetic field data. *J. Geophys. Res.* **110**, 2104.

Linker, J.A., Mikić, Z., Biesecker, D.A., Forsyth, R.J., Gibson, S.E., Lazarus, A.J., Lecinski, A., Riley, P., Szabo, A., Thompson, B.J.: 1999, Magnetohydrodynamic modeling of the solar corona during Whole Sun Month. *J. Geophys. Res.* **104**, 9809.

Liu, Y., Zhao, X., Hoeksema, J.T.: 2004, Correction of offset in MDI/SOHO magnetograms. *Solar Phys.* **219**, 39.

Liu, Y., Hoeksema, J.T., Zhao, X., Larson, R.M.: 2007, MDI synoptic charts of magnetic field: Interpolation of polar fields. In: *Bull. Am. Astron. Soc.* **38**, 129.

Luhmann, J.G., Lee, C.O., Li, Y., Arge, C.N., Galvin, A.B., Simunac, K., Russell, C.T., Howard, R.A., Petrie, G.: 2009, Solar wind sources in the late declining phase of cycle 23: Effects of the weak solar polar field on high speed streams. *Solar Phys.* **256**, 285.

Meunier, N.: 2005, Magnetic network dynamics: Activity level, feature size and anchoring depth. *Astron. Astrophys.* **436**, 1075.

Neugebauer, M., Forsyth, R.J., Galvin, A.B., Harvey, K.L., Hoeksema, J.T., Lazarus, A.J., Lepping, R.P., Linker, J.A., Mikić, Z., Steinberg, J.T., von Steiger, R., Wang, Y.M., Wimmer-Schweingruber, R.F.: 1998, Spatial structure of the solar wind and comparisons with solar data and models. *J. Geophys. Res.* **103**, 14587.

Owens, M.J., Spence, H.E., McGregor, S., Huges, W.J., Quinn, J.M., Arge, C.N., Riley, P., Linker, J., Odstricil, D.: 2008, Metrics for solar wind prediction models: comparison of empirical, hybrid and physics-based schemes with 8 years of l1 observations. *Space Weather* **6**, S08001.

Riley, P., Linker, J., Mikić, Z., Lionello, R.: 2001, MHD modeling of the solar corona and inner heliosphere: Comparison with observations. In: Song, P., Singer, H., Siscoe, G. (eds.) *Space Weather, AGU Geophys. Monogr.* **125**, 159.

Schatten, K.H., Wilcox, J.M., Ness, N.F.: 1969, A model of interplanetary and coronal magnetic fields. *Solar Phys.* **6**, 442.

Scherrer, P.H., Bogart, R.S., Bush, R.I., Hoeksema, J.T., Kosovichev, A.G., Schou, J., Rosenberg, W., Springer, L., Tarbell, T.D., Title, A., Wolfson, C.J., Zayer, I., Team, M.E.: 1995, The Solar oscillations investigation - Michelson Doppler Imager. *Solar Phys.* **162**, 129.

Schrijver, C.J., DeRosa, M.L.: 2003, Photospheric and heliospheric magnetic fields. *Solar Phys.* **212**, 165.

Svalgaard, L., Duvall, T.L. Jr., Scherrer, P.H.: 1978, The strength of the sun's polar fields. *Solar Phys.* **58**, 225.

Tran, T., Bertello, L., Ulrich, R.K., Evans, S.: 2005, Magnetic fields from SOHO MDI converted to the Mount Wilson 150 foot solar tower scale. *Astrophys. J. Suppl.* **156**, 295.

Wang, Y.M., Sheeley, N.R. Jr.: 1988, The solar origin of long-term variations of the interplanetary magnetic field strength. *J. Geophys. Res.* **93**, 11227.

Wang, Y.M., Sheeley, N.R. Jr.: 1990, Solar wind speed and coronal flux-tube expansion. *Astrophys. J.* **355**, 726.

Wang, Y.M., Sheeley, N.R. Jr.: 1992, On potential field models of the solar corona. *Astrophys. J.* **392**, 310.

Zhao, X., Hoeksema, J.T., Scherrer, P.H.: 1999, Changes of the boot-shaped coronal hole boundary during Whole Sun Month near sunspot minimum. *J. Geophys. Res.* **104**, 9735.

Table 1. Statistical evaluation of solar wind prediction from the WSA model from July 1996 to March 2009. Predictions were made using synoptic maps with the new polar field correction and the 1D interpolation. Results are based on the three-day advanced prediction and are evaluated against the OMNI data set. Four statistical measures are evaluated: root-mean-square error of the predicted speed (RMSE), mean absolute percentage error (MAPE), correlation coefficient between the predicted and observed speed (CC), and the success rate of IMF polarity prediction (PIMF).

Synoptic Map	RMSE (km s^{-1})	MAPE	CC	PIMF
New Method	96.8	0.159	0.470	0.812
1D Interpolation	104.6	0.179	0.364	0.781
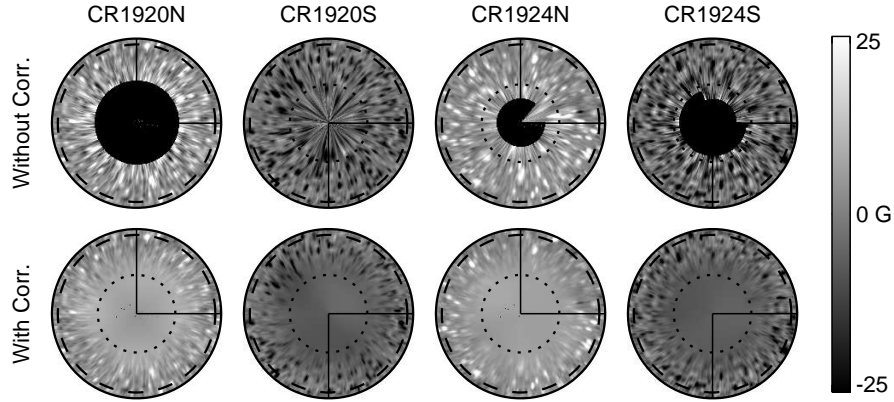
Figure 1. MDI synoptic maps of the radial field strength above 60° stereoscopically viewed from the poles: CR1920 (March 1997) and CR1924 (July 1997). In this projection, colatitude (θ) increases with the distance (R) from the pole at the center of the circle as $R \propto \tan\theta/2$, approximately linearly in this plot. Black indicates missing data. The top row shows the original data. The bottom row shows the field after interpolation. The small dotted circles indicate 75° latitude, the larger is at 62°. Horizontal solid lines show 0° Carrington longitude, vertical 90°.
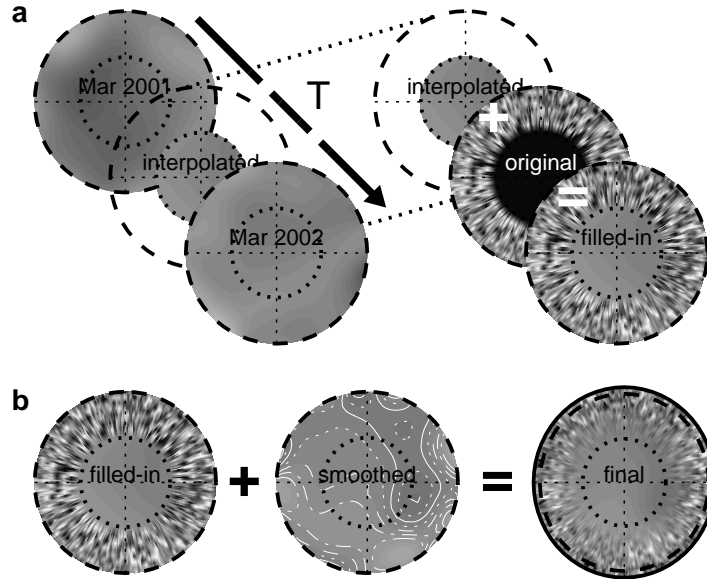
Figure 2. Illustration of the new polar field correction scheme. The circular plates are stereoscopic views of the South poles above 62° latitude. Smaller dotted circles indicate 75°. Black indicates missing data. Panel (a) shows the step of estimating the poorly measured pole-most pixels at a certain instant between March 2001 and March 2002 above 75°. The temporally interpolated values are used to replaced the pole-most pixels in observation. Panel (b) shows the process of smoothly merging the filled-in data back to the map. The observed field with gap filled is smoothed and merged back to reduce the noise level in a standard way.
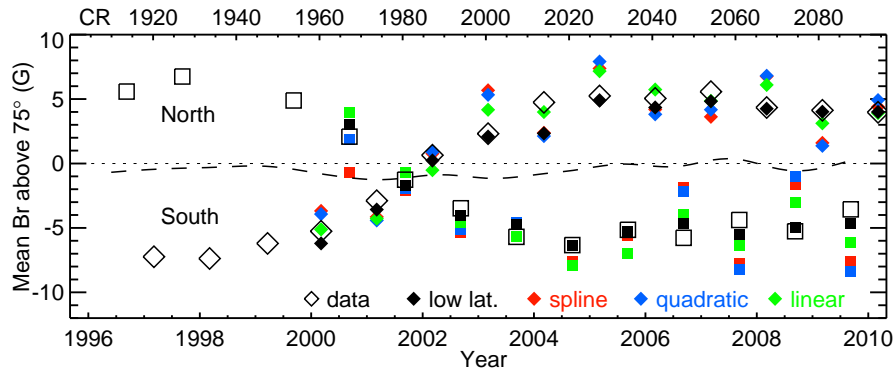

Figure 3. Comparison of four extrapolation methods for estimating the polar field strength of the next year: average from low-latitudes, cubic spline, quadratic and linear. Open squares (diamonds) indicate smoothed and averaged polar field flux density above 75° latitude in the north (south) during September (March). Each extrapolated point is based only on the data points before it. The low-latitude data are the average of the flux-density between 62° and 75° multiplied by 1.1, from the previous year. The dashed curve shows the average field strength difference between two poles after smoothing and averaging, which represents the residue imbalanced flux from polar field after the correction.
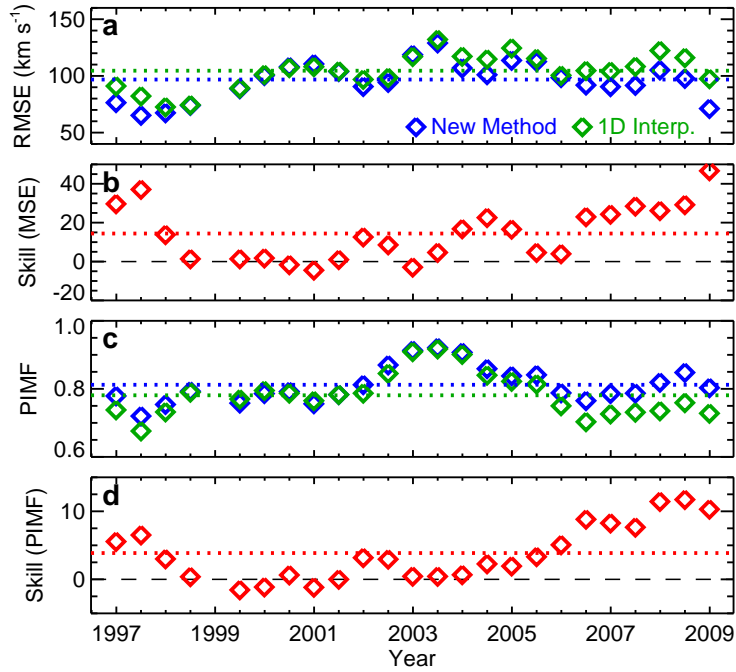
Figure 4. Statistical metrics for WSA solar wind speed and IMF polarity prediction compared with OMNI data. Results from synoptic maps with new polar field correction scheme are compared with those that use one-dimension interpolation. Each point represents a one-year window and the points are sampled every half a year. The overall average is shown as a horizontal dotted line. (a) Root mean square error (RMSE) from the new method (blue) and 1D interpolation method (green). (b) Skill score of mean square error (MSE) of the new method using the 1D method as reference. (c) Success rate of IMF polarity prediction (PIMF) from the new method (blue) and 1D interpolation method (green). (d) Skill score of the new method using the 1D method as reference.
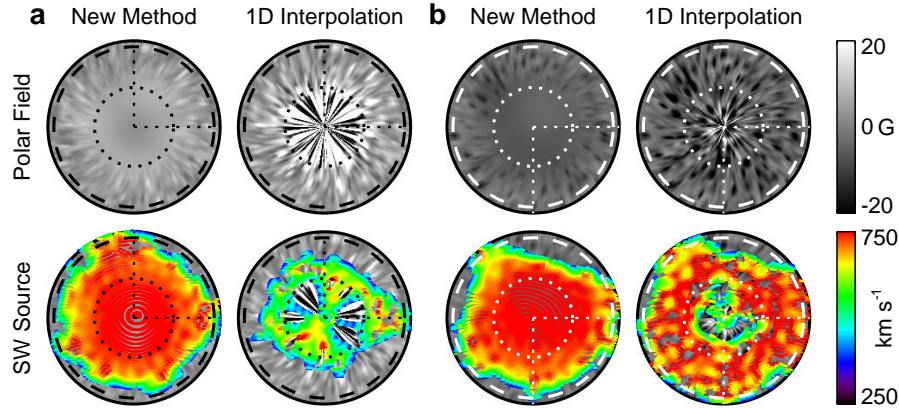
Figure 5. Comparison of derived open field line foot-points as the source location for high-latitude fast solar wind during solar minimum (CR1920), computed with new polar field correction and with 1D spatial interpolation method. (a) shows the North pole view. (b) show the South pole. In each panel, the top row shows the magnetic data after correction. The bottom shows the wind source overplotted on synoptic map, with colors indicating corresponding solar wind speed.
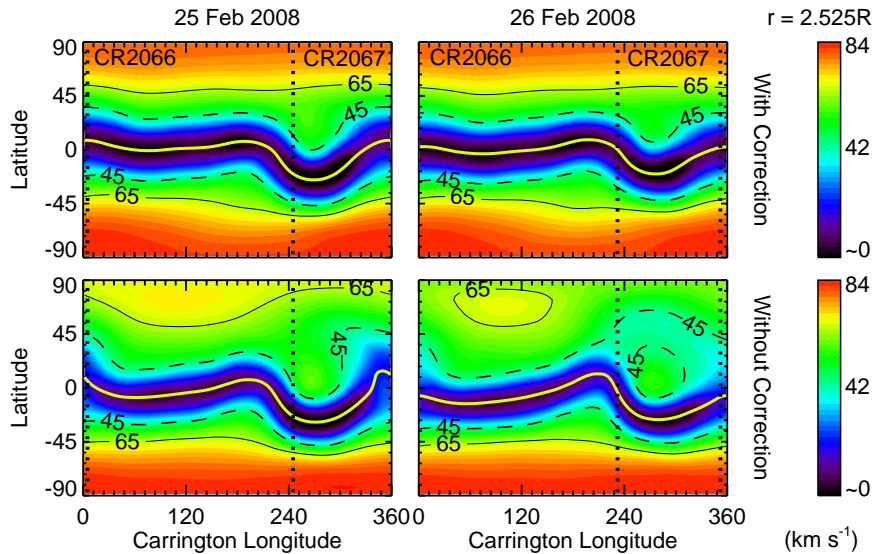

Figure 6. Solar wind speed distribution at the height of 2.525 $R_\odot$ on 25 and 26 February, 2008, derived from a daily MHD simulation with MDI daily-updated synoptic maps as input. The top row is computed using maps with new interpolation. Maps used for the bottom row are not corrected. The Carrington longitude of the central meridian passage (CMP) for these two days are 305° for and 292° respectively. The leading edge of the map is 60° east to the CMP and data within a 120° longitudinal window centered at CMP (between the two dotted lines) is updated daily with new observations. In the speed contours, lines are drawn for values of 45 and 65 to highlight the high speed regions. Due to a few "bad pixels" in the north pole region of the updated data, great changes of the solar wind speed distribution are seen over one day. In addition, the typical high speed solar wind during solar minimum is missing from the North pole.